CrystEngComm

ROYAL SOCIETY OF CHEMISTRY

PAPER

View Article Online
View Journal | View Issue

Cite this: *CrystEngComm*, 2024, **26**, 2704

A two-step method to prepare P2-type layered oxide materials for stable sodium-ion batteries *via* a precursor and sintering temperature control†

Xinhua Sun,[a] Yan Zhang,[b] Jianmin Zhang*[a] and Zongmin Zheng*[a]

With the surging demand for green energy and renewable energy, as well as the shortage and uneven distribution of global lithium resources, sodium-ion batteries are gaining increasing attention as competitive alternatives. Due to their advantages of high energy density, high safety performance and environmental friendliness, P2 layered oxides have wide application prospects as the positive electrode of sodium ion batteries. However, their practical applications face numerous obstacles due to their complex phase transitions at high voltages, leading to poor cycling stability and rate capability. In this study, a P2-type $Na_{0.67}Ni_{0.2}Mn_{0.8}O_2$ layered oxide cathode material was successfully prepared *via* a two-step method using ultra-nano-sized precursors. Meanwhile, the sintering temperature was optimized for its influence on phase as well as the electrochemical properties of cathode material for sodium-ion batteries. The materials were characterized in terms of their morphology, structure, and electrochemical properties using SEM, XRD, EDX, and galvanostatic charge–discharge tests. Compared to the traditional one-step solid-state method, the PS-900 material obtained by a two-step approach exhibited a reversible capacity of over 150 mA h g^{-1} at 0.1 C and the capacity retention reached nearly 70% after 200 cycles at 1 C. These results indicate the widespread potential application of the novel P2-type layered oxide cathode material in sodium-ion batteries.

Received 4th March 2024,
Accepted 23rd April 2024

DOI: 10.1039/d4ce00209a

rsc.li/crystengcomm

1. Introduction

With the ongoing depletion of fossil energy sources, the demand for clean energy has become increasingly pressing. In this context, the development and widespread utilization of lithium-ion batteries (LIB) is an inevitable choice in keeping with the spirit of the times.[1,2] However, on a global scale, the distribution of lithium resources is very uneven and lithium is expensive; thus, the application of lithium-ion batteries in the energy industry faces certain limitations.[3] Therefore, against this backdrop, sodium-ion batteries (SIBs) have become the focus of attention, given their abundant and cost-effective resources, thereby establishing a solid foundation for their potential as alternatives to lithium-ion batteries in the future.[4] SIBs consist of four parts: positive and negative material, electrolytes and separators, with the positive electrode material being a critical determinant of the performance of sodium-ion batteries.[5,6] At present, the mainstream cathode materials of sodium ion batteries are layered transition metal oxides, in addition to polyanionic compounds and Prussian blue analogues.[7,8] Layered metal oxides (Na_XTMO_2, where TM refers to transition metal elements such as Ni, Mn, Co, Fe, *etc.*) have garnered significant attention as a cathode material for SIBs due to their high energy density and good safety performance.[9,10] Among the prevalent layered structures, O3 and P2-type structures have garnered considerable attention.[11–13] P2-type oxides, characterized by lower sodium content and wider interlayer spacing, exhibit reduced phase transitions and enhanced rate capabilities during the electrochemical process, progressively positioning themselves as a promising option among positive electrode materials for sodium-ion batteries.[14,15] Nevertheless, when operating within a high voltage range, substantial capacity decay persists after prolonged cycling.[16]

Layered metal oxides are regarded as promising candidates with potential advantages as high-capacity cathode materials.[17] However, these electrode materials generally exhibit three major drawbacks: irreversible phase transitions,[18] storage instability,[19] and insufficient battery performance.[20] To overcome the challenges faced by layered metal oxide cathode materials, various synthesis strategies can be employed to address them. A range of methods for synthesizing positive active materials for

[a] *National Engineering Research Center for Intelligent Electrical Vehicle Power System, College of Mechanical and Electrical Engineering, Qingdao University, Qingdao, 266071, China. E-mail: zhangjm@qdu.edu.cn, zmzheng@qdu.edu.cn*
[b] *Institute of Advanced Cross-field Science, College of Life Sciences, Qingdao University, Qingdao, 266071, China*

† Electronic supplementary information (ESI) available. See DOI: https://doi.org/10.1039/d4ce00209a

SIBs have been reported including solid-state synthesis, sol–gel synthesis, and co-precipitation.[21,22] Ding *et al.*[23] successfully synthesized $Na_{0.67}Li_{0.15}Ni_{0.18}Mg_{0.02}Mn_{0.8}O_2$ material using a high-temperature solid phase method. The effect of calcination temperature on the electrochemical properties of the materials was studied comprehensively. When the voltage range is 1.5–4.2 V and the current density is 0.1 C, the discharge capacity can reach 160 mA h g^{-1} and the capacity retention rate is still maintained at 70% after 100 cycles. Gao *et al.*[24] employed the coprecipitation method to prepare the precursor, resulting in a concentration gradient during the preparation of the active material $Na_{0.65}Ni_{0.16}Co_{0.14}Mn_{0.7}O_2$ with a distinctive core–shell structure series. By utilizing this approach, the active material $Na_{0.65}Ni_{0.16}Co_{0.14}Mn_{0.7}O_2$ exhibited enhanced structural stability, a higher Na^+ diffusion coefficient, and superior electrochemical performance compared to its counterpart prepared under constant concentration conditions. Liu *et al.*[25] successfully prepared the $Na_{0.9}Ni_{0.45}Mn_{0.55}O_2$ positive electrode by the sol–gel method. They used different chelating agents to study in detail the effects of chelating agents on the morphology, structure and electrochemical properties of the samples. It was demonstrated that the samples that showed the best electrochemical properties were prepared with citric acid with a capacity of 96 mA h g^{-1} and a capacity retention rate of 48% after 300 cycles at 1 C. The suitable synthesis path and conditions directly impact the crystal structure, particle size, and uniform distribution of the active metal. These characteristics play a crucial role in determining the morphology and overall properties of the resulting active cathode material while serving as a key step in determining its final properties.[26,27]

In this study, a facile solid base phase-transition process is employed to prepare nano-sized precursors for the formation of a novel P2-type $Na0_{.67}Ni_{0.2}Mn_{0.8}O_2$ material. Compared to the traditional solid-state method, this two-step method is propitious to form a well-defined morphology and crystal structure at a relatively low sintering temperature. By using various electrochemical measurements, the materials present enhanced specific capacity, rate property and cyclic stability performance within a wide charge–discharge voltage window (1.5–4.2 V).

2. Experimental

2.1. Chemicals

In this work, the Na_2CO_3, $Mn(CH_3COO)_2{\cdot}4H_2O$, $Ni(CH_3COO)_2{\cdot}4H_2O$, and commercial MgO nanoparticles were purchased from Sinopharm Chemical Reagent Co., Ltd.; the NiO and MnO_2 powders were purchased from Aladdin and Macklin. All the reagents were used as received unless otherwise stated.

2.2. Synthesis of $Na_{0.67}Ni_{0.2}Mn_{0.8}O_2$ materials

The two-step synthesis of PS-$Na_{0.67}Ni_{0.2}Mn_{0.8}O_2$: as depicted in Fig. 1a, the first step involved a phase-transition reaction between solid base MgO and the Mn^{2+} and Ni^{2+} in a beaker under the stoichiometric ratio. After stirring for 1 h, centrifugal washing and drying, the Ni–Mn precursor (P-NM) was obtained. In the second step, the precursor and Na_2CO_3 in the stoichiometric ratio were wet-milled at 500 r min^{-1} for 2 h using a mechanical ball milling method. The as-prepared mixture was transferred to a quartz tube furnace and calcined at temperatures of 850, 900, 950, and 1000 °C in an oxygen atmosphere with a heating rate of 5 °C min^{-1} and a holding time of 12 h. The resulting materials were collected after cooling in the furnace and promptly transferred to a glove box filled with argon (the water and oxygen content were both less than 0.01 ppm) for storage. These samples were designated as PS-850, PS-900, PS-950, and PS-1000, respectively.

For comparison, as depicted in Fig. 1b, S-$Na0_{.67}Ni_{0.2}Mn_{0.8}O_2$ was prepared at 900 °C (marked as S-900) under oxygen atmosphere by sintering mixed powder containing NiO, MnO_2, and Na_2CO_3 in stoichiometric ratios.

2.3. Material characterization

X-ray diffraction (XRD, Rigaku Ultima IV) was employed to confirm the internal structure of the positive electrode material,

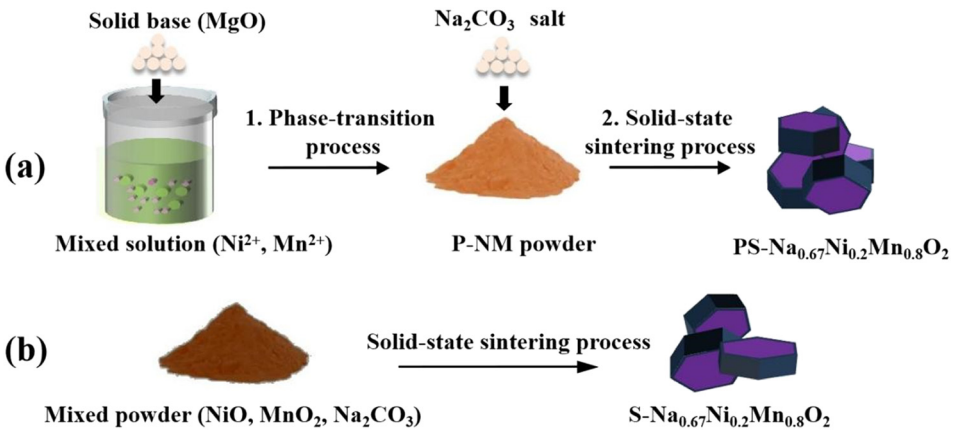

Fig. 1 Schematic illustration for the preparation process of (a) PS-$Na_{0.67}Ni_{0.2}Mn_{0.8}O_2$ and (b) S-$Na_{0.67}Ni_{0.2}Mn_{0.8}O_2$.

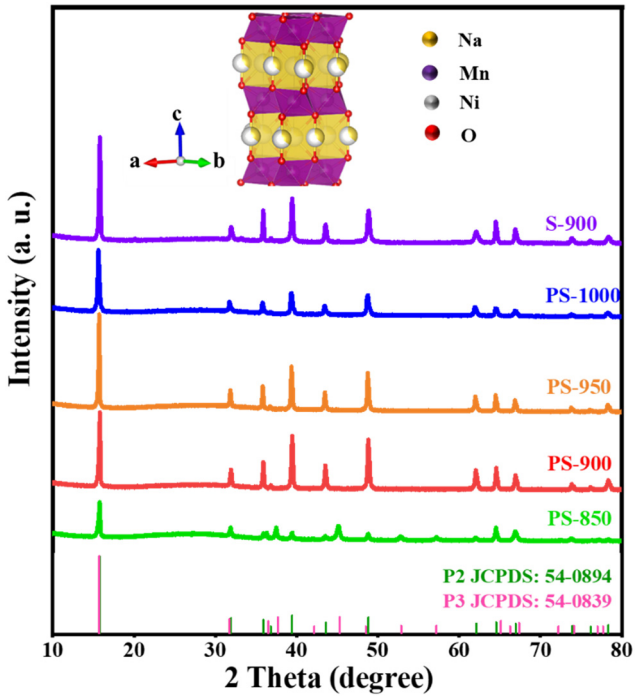

Fig. 2 The XRD pattern of all the samples with the inset showing the crystal structure of the P2 phase.

utilizing a scanning step size of 2° min^{-1} within a range of 10–80°. Furthermore, field emission scanning electron microscopy (FESEM, JSM-7800F, JEOL) was utilized to observe the surface morphology and elemental distribution of the material, coupled with energy-dispersive spectroscopy (EDS). X-ray photoelectron spectroscopy (XPS, PHI 5000 Versa Probe III) data were obtained using the PHI 5000 Versa Probe III instrument. Additionally, high-resolution transmission electron microscopy (HRTEM, JEM-2100 Plus, JEOL) was employed for in-depth crystal structure analysis.

2.4. Electrochemical properties characterization

Electrochemical testing was performed within a coin-type cell (CR2032). Initially, the weight ratio of 8 : 1 : 1 positive material, acetylene black (Super P) and polyvinylidene fluoride (PVDF) were mixed homogenously. Then, *N*-methyl-2-pyrrolidone (NMP) solvent was added and ground up to form a slurry. Subsequently, this slurry was uniformly coated onto Al foil, ensuring that the mass of the active material fell within the range of 1.6–2.6 mg cm^{-2}. After drying at 120 °C for 12 h in a vacuum oven, the coated Al foil was then cut into circular slices (a diameter of 12 mm) as cathodes. The assembly of the coin cells took place in a glove box under an argon atmosphere with oxygen and moisture content below 0.01 ppm. Sodium metal and Whatman glass fiber (GF/D) were employed as the anode and separator, respectively. The electrolyte used was 1.0 mol L^{-1} of $NaClO_4$ dissolved in a mixture of ethylene carbonate (EC) and propylene carbonate (PC) in a volume ratio of 1 : 1 with the addition of 3 wt%

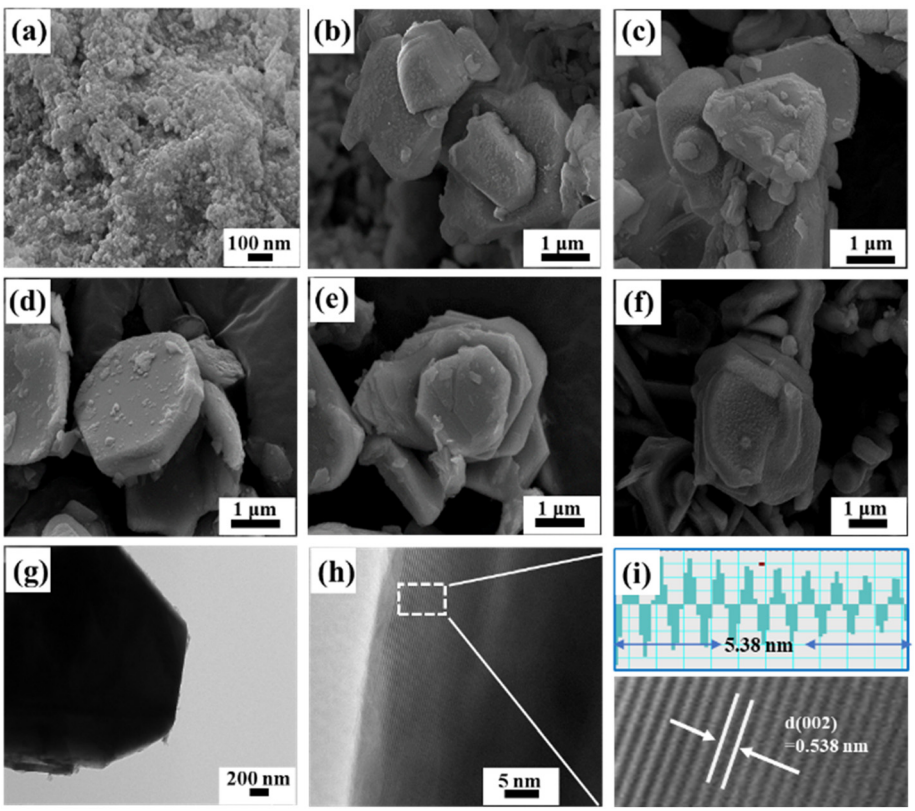

Fig. 3 The SEM images of (a) P-NM, (b) PS-850, (c) PS-900, (d) PS-950, (e) PS-1000 and (f) S-900; (g–i) the TEM and HRTEM images of PS-900.

fluoroethylene carbonate (FEC) as an additive. Constant current charge–discharge performance testing was carried out using a Neware battery tester at a voltage range of 1.5–4.2 V and a temperature of 25 ± 0.5 °C. Electrochemical impedance spectroscopy (EIS) measurements were also performed using a CHI760E electrochemical workstation with an amplitude of 5 mV and a frequency range of 10^5–10^{-2} Hz.

3. Results and discussion

The material's phase composition and crystal structure were analyzed using X-ray diffraction (XRD). The XRD pattern of the as-received precursor was shown in Fig. S1 in the ESI,† indicating a complex of Mn_3O_4 and $Ni(OH)_2{\cdot}0.75H_2O$ with a uniform distribution of Ni Mn and O elements (Fig. S2 in the ESI†). The phase analysis of the sintered samples is shown in Fig. 2. The main diffraction peaks of PS-850 can be well directed to the P2 phase of layered $Na_{0.67}Ni_{0.33}Mn_{0.67}O_2$ with a space group of $P6_3/mmc$ (JCPDS No. 54-0894). In addition, several weak peaks can be identified as a P3-type structure (JCPDS No. 54-0839).[28,29] When the calcination temperature reaches more than 900 °C, only a pure P2-type structural phase appears. As the temperature rises from 900 to 1000 °C, the intensity of the peaks decreases gradually, indicating a weak degree of crystallinity. However, the relative intensity of (002) to other crystal indices varies greatly (Table S1 in the ESI†). According to the result of the ICP analysis, the atomic ratio of Na : Mn : Ni is confirmed as expected (0.662 : 0.195 : 0.794). These results suggest that different sintered conditions greatly affect the crystal structure as well as the growth direction, which will have some effect on the electrochemical properties. Compared with the solid phase method, the two-step method has a higher mixing degree, faster reaction rate, stronger volume mass transfer effect and more homogeneous species.

The SEM images in Fig. 3 reveal that the calcination temperature significantly impacts the morphology of the $Na_{0.67}Ni_{0.2}Mn_{0.8}O_2$ powder material. As shown in Fig. 3(a), the particle size of the P-NM precursor is around ~20 nm (Fig. S3 in the ESI†), which is good for evenly mixing with the reactants. As the sintering temperature rises from 850 to 1000 °C, as shown in Fig. 3(b)–(e), the grain profile becomes clearer with a hexagonal block-like morphology. For the compared S-900 sample prepared with commercial reactants (Fig. 3(f)), the particle shape is not uniform. To further explore the structure and morphology of the PS-900, TEM and HRTEM images are presented in Fig. 3(g–i). From Fig. 3(g and h), a well-defined and hexagonal block-like crystal is identical to that in the SEM image. Through the measurement and calculation of the HRTEM image

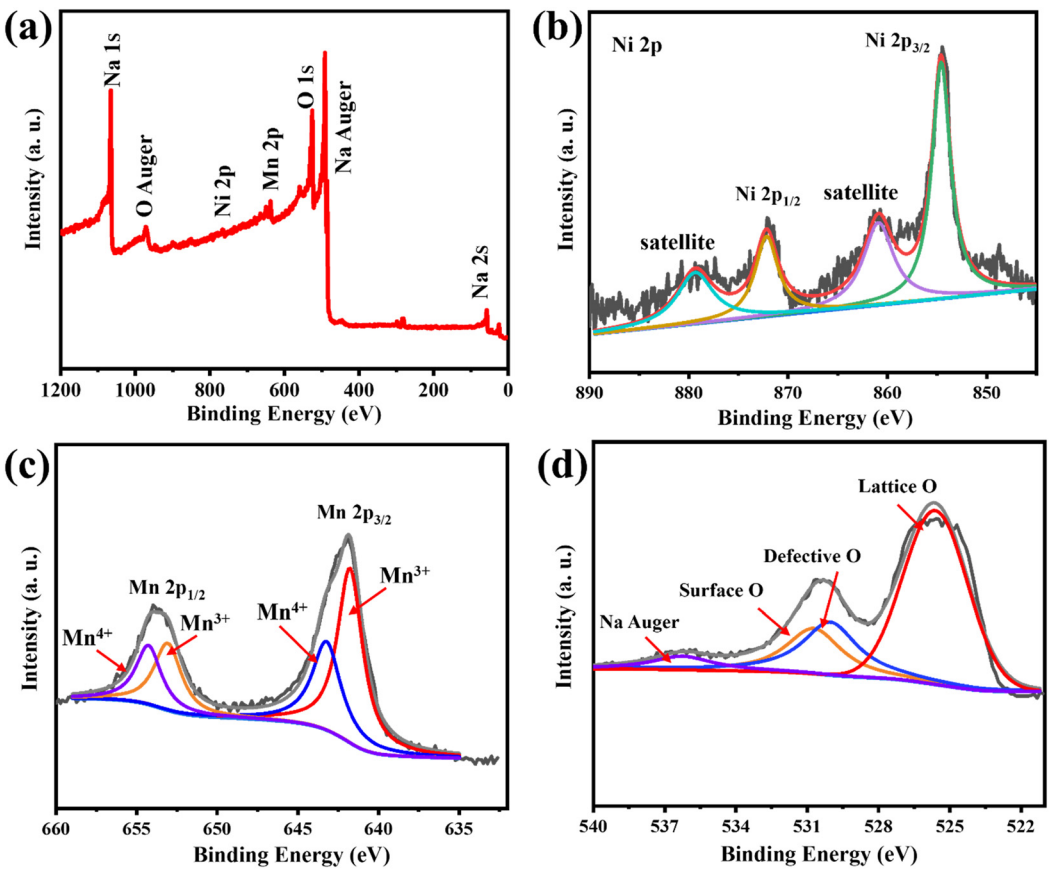

Fig. 4 The XPS spectrum of the PS-900: (a) total spectrum; (b) Ni 2p; (c) Mn 2p; and (d) O 1s.

(Fig. 3(i)), an average lattice spacing is 0.538 nm, matching with the (002) lattice plane of the P2 phase.[30]

The valence state of various elements in the PS-900 sample was investigated using X-ray photoelectron spectroscopy (XPS), as depicted in Fig. 4. The total spectrum shown in Fig. 4(a) reveals four dominant peaks, corresponding to Na 1s, Ni 2p, Mn 2p and O 1s, respectively. The Ni 2p spectrum in Fig. 4(b) displays main peaks at 854.6 and 872.1 eV attributed to Ni $2p_{3/2}$ and Ni $2p_{1/2}$, with satellite peaks at 860.8 and 879.5 eV, indicating the presence of the Ni^{2+} oxidation state.[31] As depicted in Fig. 4(c), the Mn 2p spectrum of the two samples displays two distinct peaks at approximately 637.8 eV and 648.2 eV, corresponding to Mn $2p_{1/2}$ and Mn $2p_{3/2}$, respectively. The sub-peaks observed at 641.8 and 653.0 eV are associated with Mn^{3+}, whereas those at 643.2 and 654.4 eV are linked to Mn^{4+}, suggesting the coexistence of Mn elements in both +3 and +4 oxidation states on the surface.[32] The O 1s curve in Fig. 4(d) can be divided into lattice O (525.6 eV) and oxygen vacancies containing surface O (530.8 eV) and defect O (530.0 eV). Another peak at 536.2 eV corresponds to the sodium Auger peak.[33]

To investigate the electrochemical properties of the above samples, a comparative analysis of the rate performances ranging from 0.1 to 5 C is first presented in Fig. 5. Despite receiving a high initial capacity, the PS-850 sample reacts poorly in the circularity and rate performance. Other cells show a small capacity gap at various rates. Especially, the discharge specific capacities of the PS-900 sample at current rates of 0.1, 0.2, 0.5, 1, 2, and 5 C are 150, 141, 130, 117, 98 and 65 mA h g^{-1}, respectively. Notably, a capacity retention of 64% is observed when transitioning from low current (0.1 C) to high current (5 C), followed by a recovery to 96% capacity retention upon return to low current. The detailed data of all cells is listed in Table S2 in the ESI.† Furthermore, by contrasting the charging–discharging curves of PS-900 and S-900 at various rates (Fig. 5(b) and (c)), the PS-900 sample exhibits smaller voltage polarization from low rate to high rate. Remarkably, the irreversible phase transition from P2 to O2 results in a 4.2 V platform.[34] Through the calculation of capacity resulting from the phase transformation, PS-900 has a lower percentage (2.9%) than S-900 (10.8%). To deeply analyze the difference in rate performances, the EIS tests were carried out at a scan rate of 5 mV s^{-1} after the rate tests. The obtained data was subsequently fitted to an equivalent circuit, as depicted in Fig. 5(d). Notably, analysis of the results revealed that the doped material calcined at 900 °C exhibited a reduction in the electrode–electrolyte interface charge transfer impedance (R_{ct}) in the high-frequency region, with the charge transfer

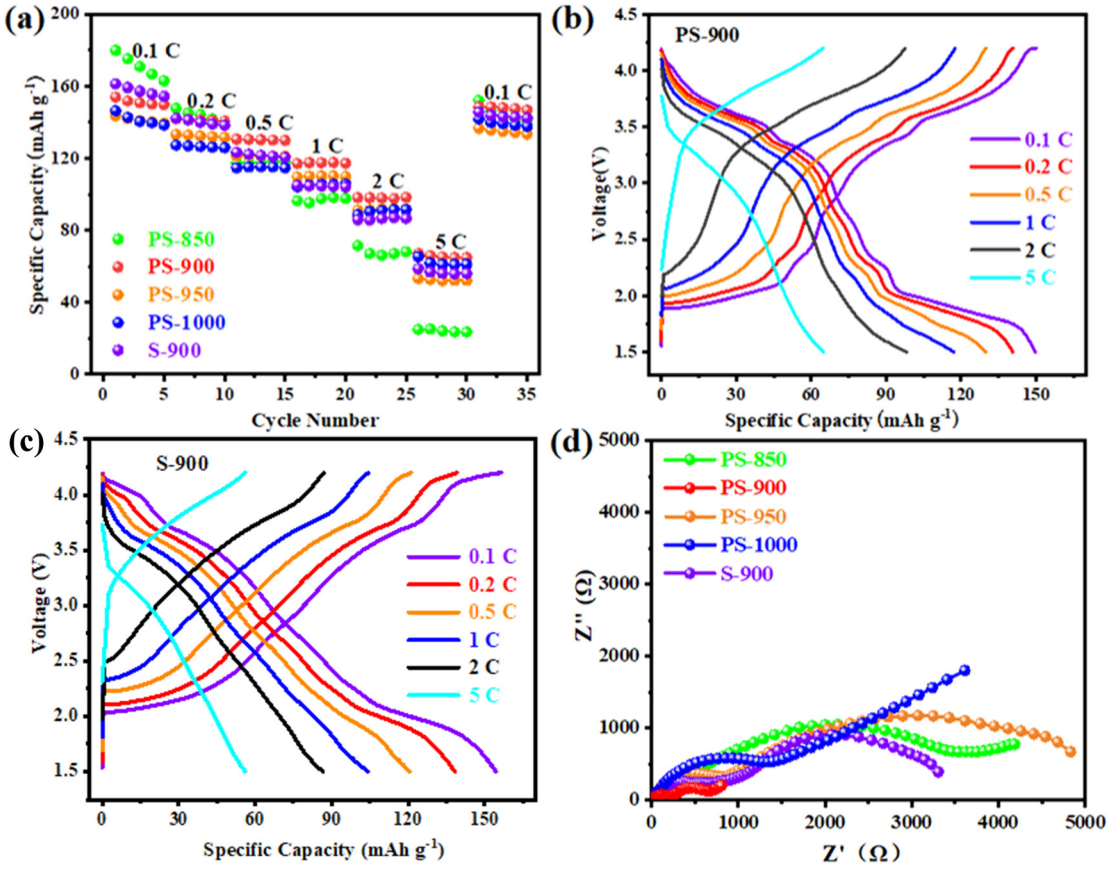

Fig. 5 (a) The rate performance of all cells at 0.1 to 5 C in the voltage range of 1.5–4.2 V, the charging–discharging curves of (b) PS-900 and (c) S-900 at various rates, and (d) the Nyquist plots of all cells at charging state after the rate tests.

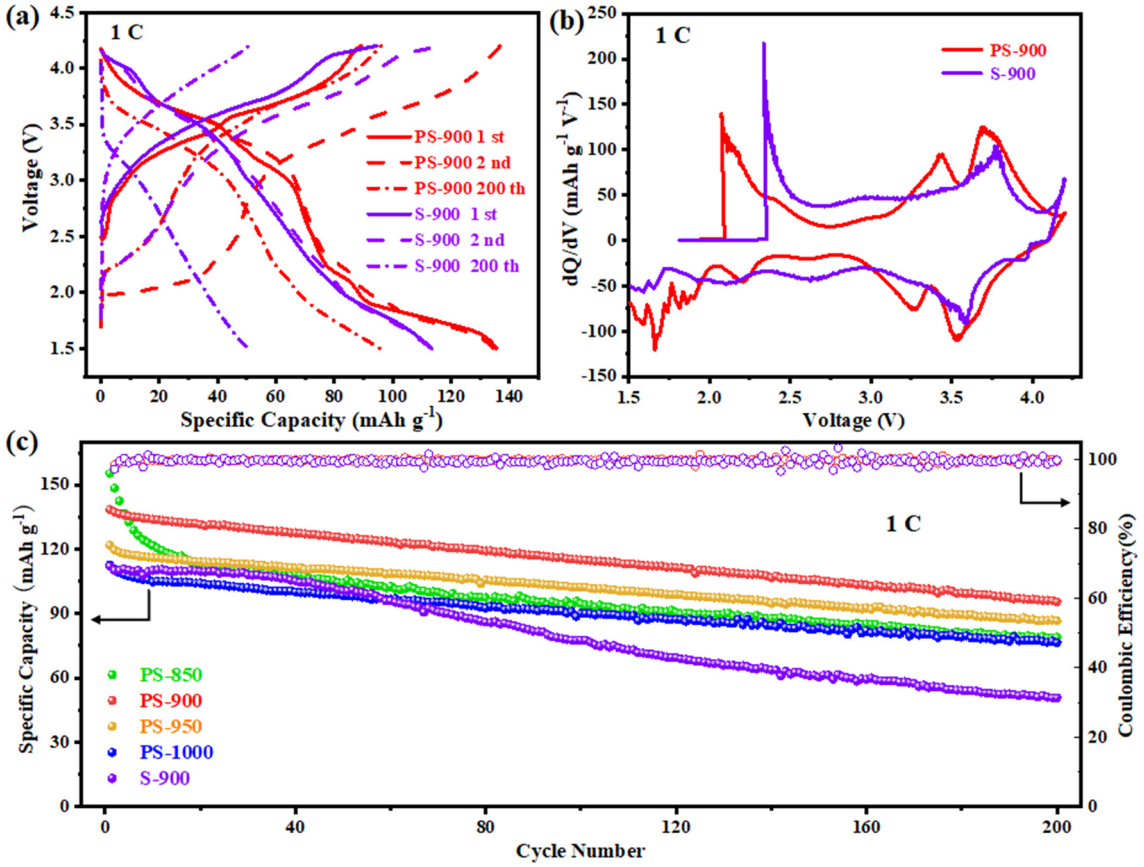

Fig. 6 (a) The galvanostatic charge–discharge curves of the 1st, 2nd and 200th cycles and (b) the dQ/dV plots (the 5th cycles) at 1 C of PS-900 and S-900 cells, respectively; (c) the long-term cyclic performance of all cells at 1 C.

impedance (R_{ct}) decreasing to 209.2 Ω. These results confirm that the sintering temperature can effectively mitigate interfacial resistance, thereby facilitating enhanced diffusion rates of electrons and ions.

Fig. 6(a) exhibits the discharge and charge profiles of the PS-900 and S-900 samples at the initial and 200th cycles at 1 C rate (based on the mass of PS-900, 1 C = 172 mA h g^{-1}). Although at such a large rate, the PS-900 sample still shows high initial specific capacity (138.5 mA h g^{-1}) and facile curves with obvious charging and discharging platform, which is proven more visually by the dQ/dV curves in Fig. 6(b). The charge voltage plateaus for PS-900 are observed at 2.07, 3.40, and 3.70 V, while the discharge voltage plateaus are noted at 2.20, 3.26, and 3.53 V. The voltage plateaus at 2.07/2.20 V are associated with the oxidation–reduction reactions of Mn^{3+}/Mn^{4+}, whereas the voltage plateaus at 3.40/3.26 and 3.70/3.53 V are linked to the oxidation–reduction reactions of Ni^{2+}/Ni^{3+} and Ni^{3+}/Ni^{4+}.[35,36] The charge voltage plateaus for S-900 are observed at 2.33, 2.96, and 3.77 V, while the discharge voltage plateaus are noted at 2.09, 2.65, and 3.59 V. The voltage plateaus at 2.33/2.09 V are associated with the oxidation–reduction reactions of Mn^{3+}/Mn^{4+}, whereas the voltage plateaus at 2.96/2.65 V and 3.77/3.59 V are linked to the oxidation–reduction reactions of Ni^{2+}/Ni^{3+} and Ni^{3+}/Ni^{4+}. It can also be seen that S-900 has a larger oxidation peak than PS-900 at around 4.2 V, indicating a phase transition. To further elucidate the cycling stability of various materials at different temperatures, long-term cyclic tests of various samples were taken at 1 C. As illustrated in Fig. 6(c), the PS-850 sample demonstrates rapid capacity degradation, particularly within the initial 40 cycles. An improvement in cyclic stability is observed with the increasing sintering temperature. Comprehensively considering capacity and retention, the PS-900 sample attains a high initial discharge capacity of 138.5 mA h g^{-1} at 1 C with a capacity retention of approximately 70% after 200 cycles, surpassing that of PS-850 (50%), PS-950 (70%), and PS-1000 (68%). In contrast, the capacity retention ratio of the S-900 sample is less than 50%. The SEM images (Fig. S4 in the ESI†) of the pole pieces before and after the cycles show that PS-900 has better structural stability.

4. Conclusions

Through a two-step synthesis method involving phase transition and solid-state reaction, the optimal P2-type layered oxide material $Na_{0.67}Ni_{0.2}Mn_{0.8}O_2$ was successfully prepared. A systematic investigation was conducted to examine the impact of calcination temperature on the structure, morphology, and electrochemical properties of the $Na_{0.67}Ni_{0.2}Mn_{0.8}O_2$ cathode material. Results from scanning electron microscopy and

transmission electron microscopy revealed a highly crystalline structure and inferior electrochemical performance of the $Na_{0.67}Ni_{0.2}Mn_{0.8}O_2$ sample at elevated temperatures. At a calcination temperature of 900 °C, the $Na_{0.67}Ni_{0.2}Mn_{0.8}O_2$ sample exhibited an initial discharge capacity of 138.5 mA h g^{-1} at a 1 C rate with a capacity retention of nearly 70% after 200 cycles. The PS-900 cathode material demonstrated outstanding cycling and rate performance, primarily attributed to the improved contact of smaller precursor grains during calcination, resulting in a more stable structure during the charge and discharge processes. This approach holds broad significance in preparing different precursors with various elements for uniform and stable sodium-ion battery cathode materials.

Conflicts of interest

The authors declare no competing financial interest.

Acknowledgements

The authors thank the financial support from the Natural Science Foundation of Shandong Province (ZR201709240128, ZR2021QB175) and the Science and Technology Small and Medium-sized Enterprises Innovation Ability Enhancement Project of Shandong Province (2022TSGC1252, 2023TSGC0754).

References

1 F. Degen, M. Winter, D. Bendig and J. Tuebke, *Nat. Energy*, 2023, **8**, 1284–1295.
2 H. Wu, P. Gao, J. Mu, Z. Miao, P. Zhou, T. Zhou and J. Zhou, *Chin. Chem. Lett.*, 2022, **33**, 3236–3240.
3 Y. Song, L. Wang, L. Sheng, D. Ren, H. Liang, Y. Li, A. Wang, H. Zhang, H. Xu and X. He, *Energy Environ. Sci.*, 2023, **16**, 1943–1963.
4 T. Yu, G. Li, Y. Duan, Y. Wu, T. Zhang, X. Zhao, M. Luo and Y. Liu, *J. Alloys Compd.*, 2023, **958**, 170486.
5 M. Yuan, H. Liu and F. Ran, *Mater. Today*, 2023, **63**, 360–379.
6 V. K. Tiwari and R. K. Singh, *Chem. Eng. J.*, 2023, **471**, 144592.
7 Y. Liu, Y.-H. Zhang, J. Ma, J. Zhao, X. Li and G. Cui, *Chem. Mater.*, 2023, **36**, 54–73.
8 C. Yang, S. Xin, L. Mai and Y. You, *Adv. Energy Mater.*, 2021, **11**, 2000974.
9 J. Huang, Z. Wu, W. Zeng, Z. Xu, L. Hu, Y. Wu and X. Lin, *CrystEngComm*, 2024, **26**, 1049–1066.
10 Y. Lai, H. Xie, P. Li, B. Li, A. Zhao, L. Luo, Z. Jiang, Y. Fang, S. Chen, X. Ai, D. Xia and Y. Cao, *Adv. Mater.*, 2022, **34**, 2206039.
11 Q. Ding, W. Zheng, A. Zhao, Y. Zhao, K. Chen, X. Zhou, H. Zhang, Q. Li, X. Ai, H. Yang, Y. Fang and Y. Cao, *Adv. Energy Mater.*, 2023, **13**, 2203802.
12 Y. Fang, X.-Y. Yu and X. W. Lou, *Angew. Chem., Int. Ed.*, 2017, **56**, 5801–5805.
13 Y. Liu, Y.-H. Zhang, J. Ma, J. Zhao, X. Li and G. Cui, *Chem. Mater.*, 2023, **36**, 54–73.
14 J. C. Kim, D.-H. Kwon, J. H. Yang, H. Kim, S.-H. Bo, L. Wu, H. Kim, D.-H. Seo, T. Shi, J. Wang, Y. Zhu and G. Ceder, *Adv. Energy Mater.*, 2020, **10**, 2001151.
15 Y. Wang, Y. Wang, Y. Xing, C. Jiang, Y. Pang, H. Liu, F. Wu and H. Gao, *J. Mater. Chem. A*, 2023, **11**, 19955–19964.
16 K. Mathiyalagan, D. Shin and Y.-C. Lee, *J. Energy Chem.*, 2024, **90**, 40–57.
17 Q. Li, B. Lin, S. Zhang and C. Deng, *J. Mater. Chem. A*, 2016, **4**, 5719–5729.
18 Z. Liu, X. Xu, S. Ji, L. Zeng, D. Zhang and J. Liu, *Chem. – Eur. J.*, 2020, **26**, 7747–7766.
19 L. Chang, R. Yang, X. Bi, W. Yang, K. Cai, A. Wei and J. Liu, *J. Energy Storage*, 2023, **73**, 109025.
20 V. P. Mhaske, S. Jilkar and M. D. Yadav, *Energy Fuels*, 2023, **37**, 16221–16244.
21 S. Majumder, R. Narasimman, S. Dhuruvan, P. Varatharajan, A. R. Murugan, S. Sarojiniamma and I. S. Appusamy, *Adv. Sustainable Syst.*, 2023, **7**, 2200519.
22 C. Hakim, N. Sabi and I. Saadoune, *J. Energy Chem.*, 2021, **61**, 47–60.
23 Y. Ding, S. Wang, Y. Sun, Q. Liu, Q. An and H. Guo, *J. Alloys Compd.*, 2023, **939**, 168780.
24 N. Gao, Y. Guo, Y. Chen, S. Feng, H. Li, R. Sun, B. Huang, S. Zhong and Q. Chen, *J. Alloys Compd.*, 2023, **958**, 170386.
25 Z. Liu, L. Li, J. Chen, H. Yang, L. Xia, J. Chen, J. Duan and Z. Chen, *J. Alloys Compd.*, 2021, **855**, 157485.
26 X. Gao, H. Liu, H. Chen, Y. Mei, B. Wang, L. Fang, M. Chen, J. Chen, J. Gao, L. Ni, L. Yang, Y. Tian, W. Deng, R. Momen, W. Wei, L. Chen, G. Zou, H. Hou, Y. M. Kang and X. Ji, *Sci. Bull.*, 2022, **67**, 1589–1602.
27 M. Li, X. Qiu, Y. Yin, T. Wei and Z. Dai, *J. Alloys Compd.*, 2023, **969**, 172406.
28 S. Su, X. Bai, L. Ming, Z. Xiao, C. Wang, B. Zhang, L. Cheng and X. Ou, *J. Solid State Chem.*, 2022, **308**, 122916.
29 Z. Yan, L. Tang, Y. Huang, W. Hua, Y. Wang, R. Liu, Q. Gu, S. Indris, S. L. Chou, Y. Huang, M. Wu and S.-X. Dou, *Angew. Chem., Int. Ed.*, 2019, **58**, 1412–1416.
30 S. Li, Y. Zhang, K. Lei, Q. Yang, Z. Liu, K. Jiang, F. Li, Q. Lu, D. Mikhailova and S. Zheng, *J. Mater. Chem. A*, 2022, **10**, 10391–10399.
31 X. Wang, X. Dong, X. Feng, Q. Shi, J. Wang, X. Yin, J. Zhang and Y. Zhao, *Small Methods*, 2023, **7**, 2201201.
32 H. Wang, Q. Liu and Y. Liu, *J. Alloys Compd.*, 2023, **962**, 171053.
33 J. L. Tian, L. R. Wu, H. J. Zhao, S. D. Xu, L. Chen, D. Zhang and X. C. Duan, *Rare Met.*, 2023, **43**, 113–123.
34 L. Xu, Q. Ran, L. Li, Q. Hu, G. Cai and X. Liu, *Electrochim. Acta*, 2023, **467**, 143085.
35 M. Li, X. Qiu, Y. Yin, T. Wei and Z. Dai, *J. Alloys Compd.*, 2023, **969**, 172306.
36 S. Majumder, R. Narasimman, S. Dhuruvan, P. Varatharajan, A. R. Murugan, S. Sarojiniamma and I. S. Appusamy, *Adv. Sustainable Syst.*, 2023, **7**, 2200519.

